

# Electronic structure and anisotropic Rashba spin-orbit coupling in monolayer black phosphorus

Z. S. Popović,\* Jamshid Moradi Kurdestany, and S. Satpathy

Department of Physics, University of Missouri, Columbia, Missouri 65201, USA

(Received 24 May 2015; published 20 July 2015)

We investigate the electronic structure of the monolayer black phosphorus (BP) using density-functional methods both with and without an applied electric field. We find that a simple one-band tight-binding Hamiltonian based on the  $p_z$  orbitals and nearest-neighbor hopping is sufficient to describe the band structure in the gap region rather well and justification for this is given from symmetry arguments. The anisotropic nature of the band structure leads in turn to an anisotropic Rashba effect, where the magnitude of the spin splitting caused by an applied electric field is not only momentum dependent, but also depends on the direction of  $\vec{k}$ . The Rashba Hamiltonian is generalized for the anisotropic case, which reads:  $H_R = \alpha_R(\vec{\sigma} \times \vec{k}') \cdot \hat{z}$ , where the scaled momentum  $\vec{k}'$  contains the anisotropy effect. The Rashba effect is studied quantitatively for BP from *ab initio* density-functional calculations in the presence of an applied electric field. A byproduct of this work is the demonstration that the strength of the spin-orbit coupling for the outermost electrons in the atoms, which are relevant for the solids, increases only as the Landau-Lifshitz  $Z^2$  scaling with the atomic number  $Z$ , rather than the higher power  $Z^4$  scaling, as sometimes thought.

DOI: 10.1103/PhysRevB.92.035135

PACS number(s): 73.22.-f, 71.70.Ej

## I. INTRODUCTION

Currently there is a considerable interest in two-dimensional (2D) materials due to their extraordinary high electronic and thermal conductivities [1,2] and a number of other unique properties, which offer the possibilities for improvement and miniaturization of electronic devices. The paradigm 2D material, graphene [3], however, lacks an electronic band gap, which poses a serious drawback for electronic applications. As a consequence, there is an emerging interest in 2D materials that are derived from the parent 3D bulk materials, which do possess a band gap. This includes the recently isolated silicene [4,5] and germanane [6], which are layered forms of silicon and germanium, the transition-metal dichalcogenides such as  $\text{MoS}_2$ , and the single-layer black phosphorus, sometimes referred to as phosphorene, which is the subject of this work.

Three-dimensional black phosphorus is a material with a long history, being known for more than a century. There are many excellent reviews [7,8] devoted to it. It is a semiconducting layered material, consisting of planes of zigzag chains stacked on top of one another to form a 3D structure, with a narrow gap of  $E_g \approx 0.30\text{--}0.35$  eV [9–11]. Today, there is a renewed interest in BP because it has a high and anisotropic mobility of charge carriers, and it has a band gap, in contrast to graphene, and the band gap is also tunable at the same time. The energy gap can be continuously tuned with applied pressure, and it reduces linearly, becoming zero around 1.7 GPa [12]. Beyond this pressure, the resistivity shows metallic behavior indicating a pressure-induced metal-insulator transition. Application of further pressure generates two reversible structural transitions: the first one, from an orthorhombic to a rhombohedral phase occurring at 5.5 GPa [13], while the second is from a rhombohedral to a simple cubic phase at about 11 GPa [14]. It is striking to note that the

compressibility along the zigzag chains, both from experiment [15] and density-functional calculations, is small as compared to the other two directions, including the  $c$  direction, along which the phosphorous planes are thought to be held together by the weak, van der Waals forces.

Recently it became possible to isolate a single layer of black phosphorus using mechanical exfoliation [16] or plasma etching [17]. This opens up the possibility for controlling the gap value by changing the number of layers. Single-layered phosphorene has a much larger band gap compared to the bulk material with its magnitude reported in the literature varying from 0.75 eV [16] to 2 eV [18]. With increasing number of layers the energy gap will gradually decrease to its bulk value.

In this paper, we study the electronic structure in the monolayer BP from density-functional calculations, giving special attention to the Rashba effect, which originates if both the spin-orbit coupling as well as an applied electric field are present. We predict a highly anisotropic Rashba splitting, which is caused by the anisotropic band structure. Based on the symmetry analysis, which shows that the electron states in the gap region are made up of mostly phosphorus  $p_z$  orbitals, we develop a one-band nearest-neighbor tight-binding model in this basis, which is found to describe the electron bands in the gap region remarkably well.

## II. ELECTRONIC STRUCTURE

### A. Crystal structure and methods

As mentioned already, BP is a layered material, with the individual layers weakly connected by van der Waals forces. The three-dimensional BP has an orthorhombic unit cell with space group  $D_{2h}^{18}$  and lattice parameters  $a = 4.38$  Å,  $b = 3.31$  Å, and  $c = 10.50$  Å [19]. Each individual BP layer consists of two parallel planes, each containing zigzag chains of phosphorous atoms with the chains extending along the  $y$  direction as shown in Fig. 1. Every phosphorus atom has three nearest neighbors, two on the same zigzag chain at a distance  $b_1$  and the third one is at a slightly different distance  $b_2$  on a different zigzag

\*Permanent address: Institute of Nuclear Sciences, Vinča, University of Belgrade, P.O. Box 522, 11001 Belgrade, Serbia.

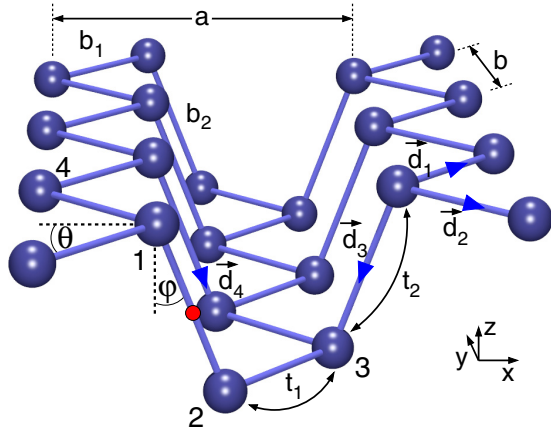


FIG. 1. (Color online) Structure of the monolayer black phosphorus. The four parameters,  $b_1$ ,  $b_2$ ,  $\theta$ , and  $\varphi$ , fully describe the geometry of the structure. The four labeled atoms form the basis of the unit cell,  $t_1$  and  $t_2$  are the two TB hopping integrals, the vector distances  $\vec{d}_i$  are used in the TB Hamiltonian, and, finally, the red dot indicates the center of symmetry.

chain located on the other plane. These two distances and the two angles  $\theta$  and  $\varphi$  shown in Fig. 1 completely describe the structure of the monolayer BP. These structural parameters corresponding to the monolayer BP in the 3D bulk material as well as those obtained for a single monolayer BP from structural optimization are presented in Table I.

For the density-functional theory (DFT) calculations, we have used the full-potential linearized augmented plane wave (LAPW) method as implemented in the WIEN2K program [20]. In this method, the trial wave function is expanded in terms of the spherical harmonics inside the muffin-tin spheres, centered around the atoms with radius  $R_{MT}$ , and for the rest of the unit cell, plane waves are used for the expansion. Throughout the calculations, the phosphorus muffin-tin radius was set to  $R_{MT} = 2.04$  a.u. The maximum length for the reciprocal vector  $K_{max}$  was chosen such that  $R_{MT}K_{max} = 8$ . This parameter determines the number of plane waves used and the size of the Hamiltonian matrix, which is in our case 2265 for the  $\Gamma$  point and similarly for the other  $\vec{k}$  points. For the integration over the Brillouin zone (BZ) we used the tetrahedron method with a mesh of 40  $\vec{k}$  points in the irreducible BZ. We used the generalized gradient approximation (GGA) with the

TABLE I. Structural parameters for the monolayer BP,  $b_1$ ,  $b_2$ ,  $\theta$ , and  $\varphi$ , as defined in Fig. 1. The planar lattice constants are given by  $a = 2b_1 \sin \theta$ , and  $b = 2b_1 \cos \theta + 2b_2 \sin \varphi$ .

	3D bulk structure	Monolayer BP (optimized)
$b_1$ [Å]	2.170	2.243
$b_2$ [Å]	2.204	2.261
$\theta$	49.74°	48.41°
$\varphi$	20.96°	21.41°
$a$ [Å]	4.38	4.626
$b$ [Å]	3.31	3.356

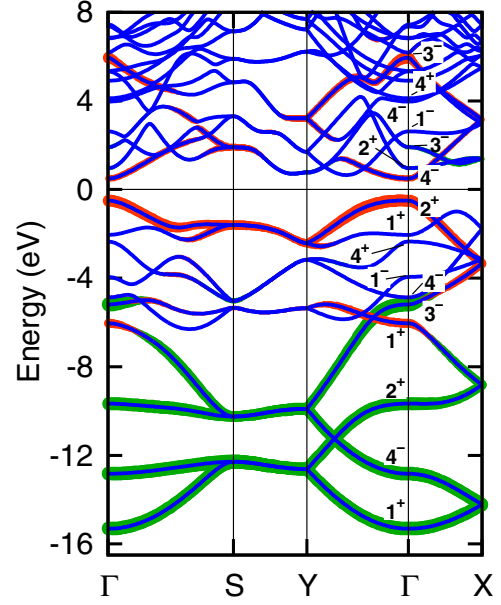


FIG. 2. (Color online) The DFT band structure for the monolayer BP, along with projected contributions from the  $s$  (green),  $p_z$  (red), and  $p_x/p_y$  (blue) orbitals. The symmetry points are:  $S = \pi(1/a, 1/b)$ ,  $X = \pi(1/a, 0)$ ,  $Y = \pi(0, 1/b)$ . These bands are without SOC and the symmetry labels at the  $\Gamma$  point are single representations as listed in Table II. Bands with SOC don't look any different on this scale, since SOC is small for phosphorus.

Perdew-Burke-Ernzerhof functional [21] for the exchange-correlation energy.

Our calculations for the monolayer BP were made in the supercell configuration with a large  $c$  axis normal to the layers (typically  $\gtrsim 20$  Å), so that there is negligible interaction between the BP layers. Starting from the atomic positions of the monolayer BP taken from the bulk 3D structure, we optimized the atomic positions until the forces became  $\lesssim 10$  mRy/Å. The results are presented in Table I. As seen from the table, the new values of the planar lattice constants show a large expansion normal to the zigzag chains,  $a = 4.626$  Å, and a moderate expansion along the zigzag chain,  $b = 3.356$  Å, consistent with earlier results in the literature [22]. For ready reference, we quote the coordinates of the four atoms in the unit cell, which are  $\vec{r}_{1,2} = \pm(-\sin \varphi, 0, \cos \varphi) b_2/2$ ,  $\vec{r}_{3,4} = (\pm \cos \theta, \sin \theta, 0) b_1 \pm (\sin \varphi, 0, -\cos \varphi) b_2/2$ , measured from the center of symmetry, marked by a red dot in Fig. 1.

## B. Density-functional electronic structure

The calculated band structure is shown in Fig. 2. The symmetry labels at the  $\Gamma$  point were obtained by examining the symmetry of the individual wave functions with respect to the various symmetry operations of the  $D_{2h}$  point group, which is the symmetry at the  $\Gamma$  point of the Brillouin zone in the monolayer BP. These symmetries provide valuable information regarding the bonding and the nature of the electron states as discussed below. The symmetry notations are the same as used by previous authors and are listed in the Appendix [23,24].

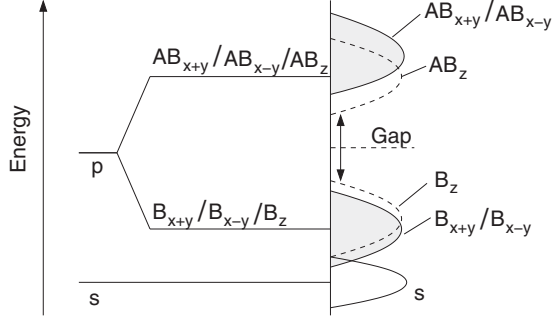


FIG. 3. Schematic electronic structure as extracted from the DFT calculations. Energies are not to scale.

The basic electronic structure that emerges from the DFT results is shown schematically in Fig. 3. The overall band structure can be described in terms of the occupation of the covalent  $p$ - $p$  bonds along the three bonds joining a phosphorus atom to its neighbors, while the antibond states are empty. The strong  $p$ - $p$  covalent character of the P-P bonds is clearly seen from the valence charge density plot, Fig. 4. The three covalent  $p$ - $p$  bonds accommodate six electrons or three per phosphorus atom, while the  $s$  orbitals are fully occupied, leading to the nominal chemical valence of  $P(s^2p^3)$ . As seen from the band structure, Fig. 2, and also from the partial density of states (DOS), Fig. 5, the electron states near the valence band maximum and the conduction band minimum are made primarily of  $p_z$  orbitals.

A symmetry analysis provides considerable insight into the nature of the electron states. Table II shows the irreducible representations of the  $D_{2h}$  point group, spanned

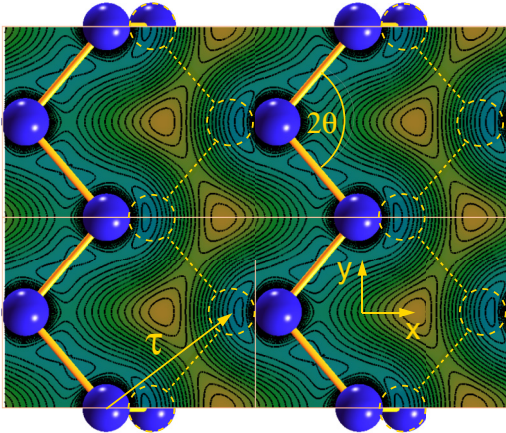


FIG. 4. (Color online) Charge density contours of the occupied valence band states (within the energy window of  $E_F$  and  $E_F - 1$  eV) on the top plane containing half of the zigzag chains obtained from the DFT calculations. The zigzag chains on the bottom plane are indicated by the light, dashed lines. The maximum charges occur on the bond centers, indicating their strong covalent character. The center of symmetry is at the midpoint of the line joining a blue atom with the adjacent dashed-line atom, which occurs on the plane below. The various symmetry elements indicated in the Appendix are best visualized using this figure, and the vector  $\vec{\tau} = (a/2, b/2)$ , which lies on the  $x$ - $y$  plane, indicates the fractional translation.

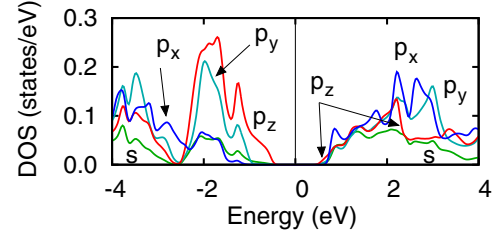


FIG. 5. (Color online) Partial densities of states (DOS) for the monolayer BP, indicating that the low-energy electron states in the gap region consist predominantly of  $p_z$  orbitals.

by the phosphorus-based orbitals of angular momentum  $l = s, p$ , and  $d$  as well as those spanned by objects that have the symmetries of the P-P bonds. For concreteness,  $B_{x+y}, B_{x-y}, AB_{x+y}$ , and  $AB_{x-y}$  are bonding or antibonding states made out of  $p_{\hat{x} \pm \hat{y}}$  orbitals pointed along  $\hat{x} \pm \hat{y}$  directions, i.e., along the zigzag line, while  $B_z$  and  $AB_z$  are the same along the interplanar bonds connecting the two planes.  $B_z/AB_z$  can have admixtures from the  $p_x$  orbitals in order for them to be aligned along the interplanar bonds, which are tilted from the  $\hat{z}$  direction. In the present case, symmetry properties are the same whether we make  $B_z/AB_z$  combinations out of pure  $p_z$  orbitals or from  $p$  orbitals that are pointed along the P-P interplanar bonds. Tilting the  $p_z$  orbitals would require a small admixture of  $p_x$ , viz,  $p_z = \cos \varphi p_z + \sin \varphi p_x \approx 0.93 p_z + 0.36 p_x$ ,  $\varphi$  being  $\sim 21^\circ$  in the present case, i.e.,  $p_x$  contribution is only about 10 % to the charge density  $|\Psi|^2$ , in order for the tilted orbital  $p_z$  to point along the interplanar P-P bond. The DFT results confirm this picture. We find that the valence top wave function has the charge components  $|\Psi(\Gamma_2^+)|^2 = 0.06 s + 0.04 p_x + 0.00 p_y + 0.90 p_z$ , while for the conduction bottom, it is  $|\Psi(\Gamma_4^-)|^2 = 0.14 s + 0.21 p_x + 0.00 p_y + 0.65 p_z$ . Note that the  $s$  contribution to these wave functions is relatively small, as these states have energies far below the gap region, while the  $p_y$  contribution is exactly zero, as dictated by symmetry presented in Table II.

The irreducible representations spanned by the various orbitals shown in Table II are consistent with the symmetry of the wave functions indicated in the band structure plot, Fig. 2. The four P- $s$  orbitals in the unit cell span the representations  $\Gamma(s) = \Gamma_1^+ + \Gamma_2^+ + \Gamma_3^- + \Gamma_4^-$ , which are clearly identifiable occurring towards the lower part of the valence bands,

TABLE II. Irreducible representations of the  $D_{2h}$  point group spanned by the atom-centered as well as bond-centered phosphorus orbitals at the  $\Gamma$  point. Here,  $N$  = number of orbitals in the unit cell, and the bond/antibond ( $B/AB$ ) orbitals are defined in the text.

Orbitals	N	$\Gamma_1^+$	$\Gamma_2^+$	$\Gamma_3^+$	$\Gamma_4^+$	$\Gamma_1^-$	$\Gamma_2^-$	$\Gamma_3^-$	$\Gamma_4^-$
$s$ or $p_x$ or $p_z$	4	1	1					1	1
$p_y$	4			1	1	1	1		
$d$	20	3	3	2	2	2	2	3	3
$B_z$	2	1	1						
$AB_z$	2							1	1
$B_{x+y}, B_{x-y}$	4	1			1	1			1
$AB_{x+y}, AB_{x-y}$	4			1	1		1	1	



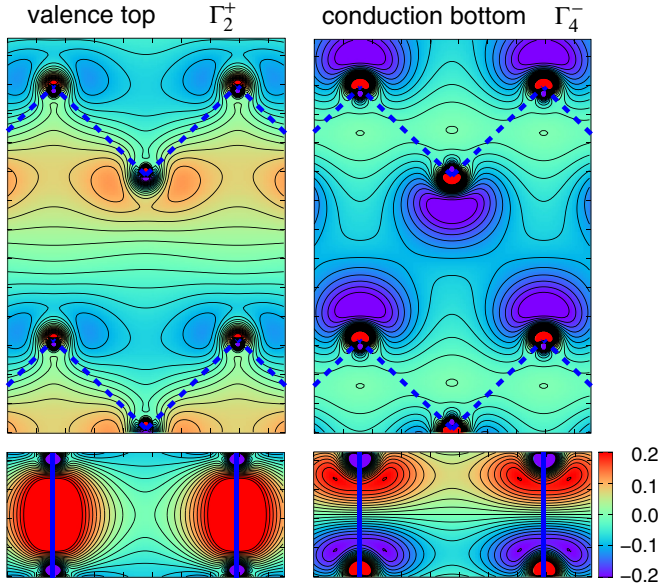


FIG. 6. (Color online) Contour plot of the wave function of the valence band top (left) and conduction band bottom (right). Both wave functions are shown on the upper zigzag plane (top) and on the plane containing the interplanar P-P bonds (bottom). The wave functions on the lower zigzag plane, not shown here, are readily obtained using inversion symmetry (the  $\Gamma_2^+$  state is inversion symmetric, while  $\Gamma_4^-$  is inversion antisymmetric, as clear from the bottom figures, where the pairs of atoms forming the bonds are related by inversion symmetry). The uppermost two atoms in the top and bottom figures are the same atoms.

indicating that the  $s$  orbitals are more or less fully occupied. The bond orbitals on the zigzag chains  $B_{x+y}$ ,  $B_{x-y}$  transform among one another under the symmetry operations of the group, spanning a four-dimensional representation, which may be reduced as  $\Gamma = \Gamma_1^+ + \Gamma_4^+ + \Gamma_1^- + \Gamma_4^-$ , and these are again exactly the same symmetries spanned by the valence bands derived from the  $p_x/p_y$  orbitals as seen from Fig. 2. The

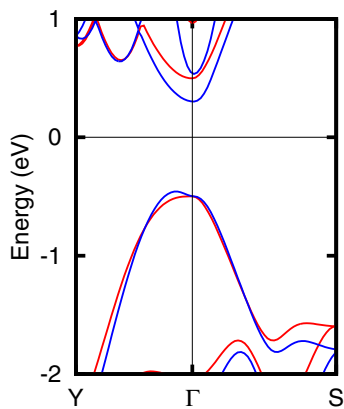


FIG. 7. (Color online) Comparison of electron bands for the unoptimized (blue) vs optimized (red) structure (structural parameters presented in Table I). An important difference is the band dispersion near the valence band top, that can lead to direct or indirect gap depending on atom positions.

TABLE III. Hopping integrals  $t_1$  and  $t_2$  obtained by fitting the TB bands with the DFT gaps or the experimental gaps,  $E_g$  and  $\Delta_X$ , as indicated in Fig. 8.

	$t_1$	$t_2$	$E_g$	$\Delta_X$
DFT	-0.95	2.40	1.00	6.12
Exp.	-0.97	2.71	1.55	6.67

antibonding combination  $AB_{x+y}$ ,  $AB_{x-y}$  span totally different irreducible representations and don't mix with the  $B_{x+y}$ ,  $B_{x-y}$  orbitals at the  $\Gamma$  point.

The valence top and conduction bottom wave functions at  $\Gamma$  are made up of, respectively, bonding and antibonding combinations of  $p_z$  orbitals, i.e.,  $B_z$  and  $AB_z$ . As seen from Table II, the  $B_z$  orbitals, two per cell, span the irreducible representations  $\Gamma = \Gamma_1^+ + \Gamma_2^+$ , while the  $AB_z$  orbitals span the  $\Gamma = \Gamma_3^- + \Gamma_4^-$  combinations, all of which are clearly seen in the band structure, Fig. 2. Note that from symmetry point of view, the  $B_z$  and  $AB_z$  could be made out of not just  $p_z$ , but also could be combined with  $s$  or  $p_x$  orbitals, but mixture with  $p_y$  is forbidden from symmetry, as already mentioned. The  $s$  orbitals are too far away in energy, so they don't contribute much, but from geometry, one expects a significant mixture from the  $p_x$  orbitals, in order that the combined  $p_z$  orbitals can tilt along the P-P interplanar bond. This is clear from the wave functions  $\Psi(r)$  plotted in Fig. 6, where a strong interplanar P-P bond is seen for the valence top state and a P-P antibond for the conduction bottom state.

There is a difference in the results presented in the literature regarding whether the band gap in the monolayer BP is direct or indirect. We find that the band gap is direct for the optimized structure, although the calculated magnitude  $E_g = 1.0$  eV is smaller than the measured value of 1.55 eV obtained from optical measurements [22], which is the usual underestimate of the band gaps in the DFT calculations. In contrast, the gap

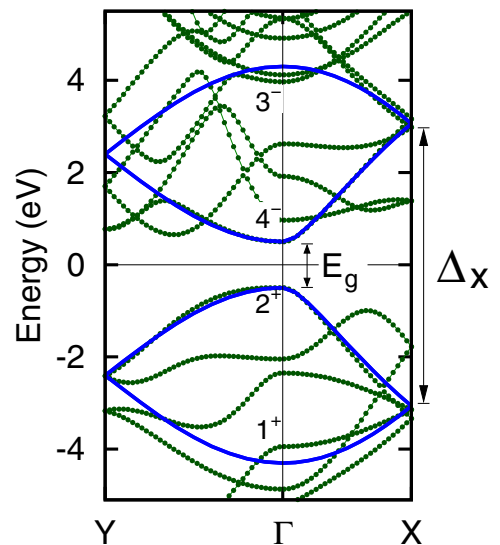


FIG. 8. (Color online) Tight-binding bands (blue lines) as obtained from Eq. (2) compared with the DFT bands (green dots). TB parameters are:  $t_1 = -0.95$  eV and  $t_2 = 2.40$  eV.

is indirect for the unoptimized structure (structural parameters the same as in 3D BP), with the valence top slightly offset from the  $\Gamma$  point along the  $\Gamma$ -Y line (Fig. 7), as has been reported in some works [25], presumably using the unoptimized structure. Results presented throughout this paper are for the optimized structure, which results in a direct gap.

### C. Tight-binding model

It is clear from the above analysis of symmetry and orbital characters of the wave functions that a tight-binding (TB) model involving just the tilted “ $p_z$ ” orbitals ( $p$  orbital lobes oriented along the interplanar P-P bond) should be able to describe the band structure in the gap region, both the valence band top as well as the conduction band bottom. We find that this is the case and moreover that the low-energy states

in the gap region are described remarkably well by keeping just the nearest-neighbor interactions, with only two hopping parameters  $t_1$  and  $t_2$  as shown in Fig. 1. We did not find significant improvement of the bands if we retained higher neighbor TB hoppings. If a description of the band structure beyond the low-energy states in the gap region is desired, then one must retain the  $p_x$  and the  $p_y$  orbitals as well as the higher neighbor interactions.

In the basis set of the four sublattice Bloch functions made out of the four phosphorus “ $p_z$ ” orbitals in the unit cell,  $c_{k\alpha}^\dagger = \mathcal{N}^{-1/2} \sum_i e^{i\vec{k}\cdot\vec{r}_{i\alpha}} c_{i\alpha}^\dagger$ , where  $c_{i\alpha}^\dagger$  creates a “ $p_z$ ” orbital at the  $\alpha$ th site in the  $i$ th unit cell,  $\vec{k}$  is the Bloch momentum, and  $\vec{r}_{i\alpha} = \vec{R}_i + \vec{\tau}_\alpha$  is the orbital position, the TB Hamiltonian is given by  $\mathcal{H}_{\alpha\beta}(\vec{k}) = \sum_i e^{i\vec{k}\cdot\vec{d}_{i\alpha\beta}} \langle 0, \alpha | \mathcal{H} | i, \beta \rangle$ , where distance  $\vec{d}_{i\alpha\beta} \equiv \vec{r}_{i\beta} - \vec{r}_{0\alpha}$  and  $\langle 0, \alpha | \mathcal{H} | i, \beta \rangle$  are the hopping integrals.

The Hamiltonian is readily found to be

$$\mathcal{H}(\vec{k}) = \begin{pmatrix} 0 & t_2 e^{i\vec{k}\cdot\vec{d}_4} & 0 & t_1(e^{-i\vec{k}\cdot\vec{d}_1} + e^{-i\vec{k}\cdot\vec{d}_2}) \\ t_2 e^{-i\vec{k}\cdot\vec{d}_4} & 0 & t_1(e^{i\vec{k}\cdot\vec{d}_1} + e^{i\vec{k}\cdot\vec{d}_2}) & 0 \\ 0 & t_1(e^{-i\vec{k}\cdot\vec{d}_1} + e^{-i\vec{k}\cdot\vec{d}_2}) & 0 & t_2 e^{-i\vec{k}\cdot\vec{d}_3} \\ t_1(e^{i\vec{k}\cdot\vec{d}_1} + e^{i\vec{k}\cdot\vec{d}_2}) & 0 & t_2 e^{i\vec{k}\cdot\vec{d}_3} & 0 \end{pmatrix}, \quad (1)$$

where  $t_1$  and  $t_2$ , again, are the nearest-neighbor hopping integrals and  $\vec{d}_{1,2} = (\cos \theta, \pm \sin \theta, 0)$ ,  $\vec{d}_{3,4} = (\mp \sin \varphi, 0, -\cos \varphi)$   $b_2$  are distances, all shown in Fig. 1.

The Hamiltonian is easily diagonalized to yield the result

$$\varepsilon(\vec{k}) = \pm \sqrt{t_2^2 + 4t_1^2 \cos^2 \frac{k_y b}{2}} \pm 4t_1 t_2 \cos \frac{k_x a}{2} \cos \frac{k_y b}{2}. \quad (2)$$

We have obtained the two parameters  $t_1$  and  $t_2$  by simply fitting the two gap values at the  $\Gamma$  and  $X$  points,  $E_g(\Gamma) = 2t_2 + 4t_1$ , and  $\Delta_X = 2\sqrt{t_2^2 + 4t_1^2}$ , with either the DFT results or the experimental values [22]. The fitted parameters are listed in Table III. The agreement of the TB results with the DFT bands, shown in Fig. 8, is remarkable considering the simplicity of the model.

### Anisotropic conductivity

The isoenergy contours for both valence and conduction bands are anisotropic, as seen for the valence bands from Fig. 9. From the band structure, we extract the following effective masses for the electrons and holes:  $m_x^*(h) = 0.16$ ,  $m_y^*(h) = 5.5$ ,  $m_x^*(e) = 0.17$ , and  $m_y^*(e) = 1.26$ , which are in agreement with earlier calculations [22]. The effective mass for the hole states in the  $y$  direction has the largest value, but we find that it is rather sensitive not only to the functional used in the DFT calculations, but also on the atomic positions, i.e., whether optimized or unoptimized (see Fig. 7).

The large anisotropy in the effective mass shows up in the measured conductivity. We focus on the  $p$ -doped samples, for which resistivity data exists. The measured conductivity is larger along the direction normal to the zigzag chains as compared to parallel to the chains,  $\sigma_x > \sigma_y$ . However, the monolayer BP is rather sensitive to environmental influence and resistivities have been measured only for films thicker than

$\sim 3$  nm [16]. Even for these thick films, due to fringing effects, the measured ratio of  $\sigma_x/\sigma_y$  was only qualitatively found to be anisotropic by about 50%. The resistivity in the bulk samples have however been studied quite early on [12,26,27] and the measured conductivity ratio in the planar direction is  $(\sigma_x/\sigma_y)_{\text{exp}} = 2.46$  [28].

Using the kinetic transport theory, the conductivity may be connected to the effective masses and the relaxation times. According to this theory, the conductivity is given by  $\sigma = \frac{1}{3} \tau e^2 \langle v_f^2 \rangle N_f$ , where  $\tau$  is the relaxation time,  $v_f$  is the Fermi velocity, and  $N_f$  is the electron density at the Fermi

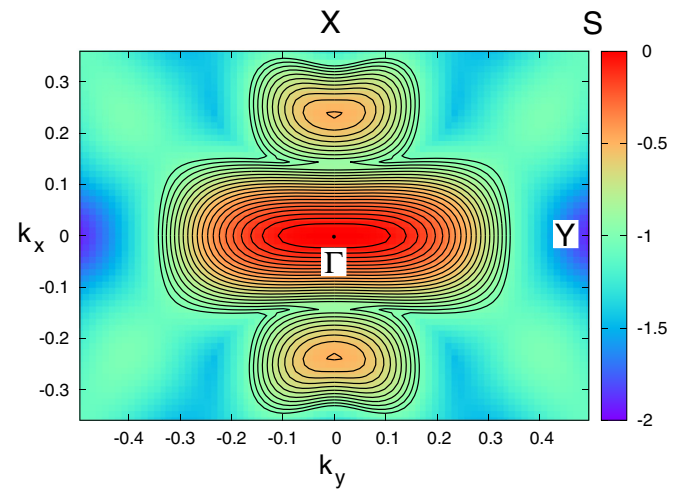


FIG. 9. (Color online) Energy contours for the topmost valence band, obtained from the DFT calculations, indicating highly anisotropic Fermi surface for  $p$ -doped BP, with hole effective masses  $m_y^*/m_x^* \approx 34$ . The energy of the valence band top at  $\Gamma$  is taken as zero and contour lines have been drawn up to  $E = -1$  eV.

energy. It is reasonable to expect the relaxation time to be anisotropic as well, considering the anisotropy in the structure and the phonon energies. However, its value is not known and is difficult to estimate theoretically. We have computed  $\sigma/\tau$  using DFT and the kinetic transport theory and from the experimental value of  $\sigma$ , estimated the relaxation time. The Fermi velocity average  $\langle v_f^2 \rangle$  can be estimated by assuming the rectangular shape for the isoenergy contours, as seen from Fig. 9. For each side of the rectangular constant-energy contour, one component of the velocity is zero, which yields the simple result:  $\langle v_y^2 \rangle / \langle v_x^2 \rangle = m_x^* / m_y^* \approx 34$ . Putting together all these, we find the ratio  $\tau_y \approx 14\tau_x$ . This is qualitatively similar to earlier estimates [29], but quantitatively different. As noted earlier, the  $m_y^*$  is sensitive to atom positions and hence differs quite a bit between different calculations in the literature.

### III. ELECTRIC FIELD AND RASHBA EFFECT

Relativistic effects in solids are usually small and often neglected, but in 2D materials they may play an important role, especially if the material is placed in an external electric field or on a polar substrate. For example, the spin-orbit coupling in graphene is quite small, but it induces important changes, e.g., massless Dirac electrons acquire a finite mass and a small gap opens up in the energy spectrum [30]. Recently it was also observed that attachment of small amounts of hydrogen adatoms on graphene can increase the SOC by three orders of magnitude [31]. The other possible way to significantly amplify the SOC is to place graphene on a polar substrate with a large Rashba-type splitting, which has been investigated both experimentally and theoretically [32].

Phosphorus is a heavier element compared to carbon implying that the effects of the SOC in black phosphorus are more pronounced than it is in graphene. In this section, we study the effect of the application of an external electric field on monolayer BP from density-functional calculations. In the presence of the SOC, the electric-field-induced broken inversion symmetry leads to the Rashba effect [33,34], which is the linear momentum-dependent spin splitting of the band structure, which we study for monolayer BP in the remaining part of the paper.

The strength of the spin-orbit coupling in atoms increases roughly quadratically (Landau-Lifshitz  $Z^2$  scaling) [35,36] with the atomic number  $Z$ , if we consider the outermost electrons in the atom, which are the relevant electrons in the solid. Thus, we have,  $\mathcal{H}_{SO} = \lambda \vec{L} \cdot \vec{S}$ , with  $\lambda = A\alpha^2 Z^2$  Ry, where  $\alpha$  is the fine structure constant, and  $A$  is of the order of one.

This scaling is illustrated in Fig. 10 where we have plotted  $\lambda$  for various atoms as calculated by Herman and Skillman [37] using the Hartree-Fock method. These data are very similar to those calculated by other authors, e.g., by Andersen, *et al.* [38], in the context of the SOC in solids. From the figure, one sees the rough  $Z^2$  dependence for the outermost electrons (i.e., without any reference to the  $n, l$  quantum numbers), while  $\lambda$  scales as the hydrogenic result  $Z^4$  within a series, i.e., where we fix the quantum numbers  $n$  and  $l$  [39]. Thus, e.g., within the  $5d$  series, as one goes from Lu to Au, the SOC parameter  $\lambda$  increases as  $Z^4$ , while as one goes from Sc to U, the outermost electrons have changed their  $n, l$  values, and  $\lambda$  increases roughly as  $Z^2$ .

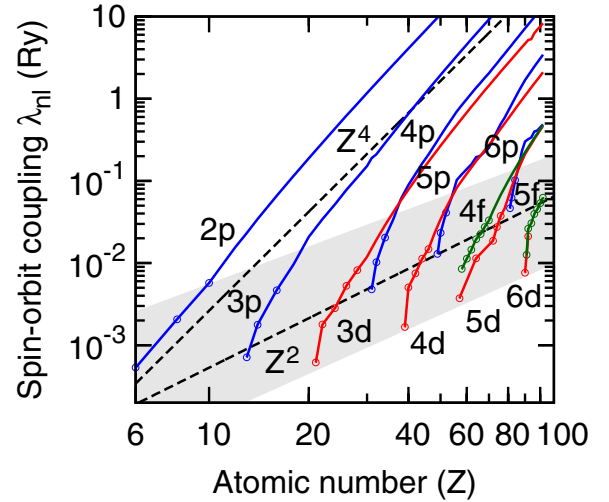


FIG. 10. (Color online) The spin-orbit coupling strength  $\lambda_{nl}$  for atoms as a function of the atomic number  $Z$ . Within a series with fixed  $n, l$  quantum numbers,  $\lambda$  follows the hydrogenic  $Z^4$  dependence, while if we consider the outermost electrons in the atom, irrespective of their  $nl$  values, (indicated by the circles and the shaded area), it increases only as the Landau-Lifshitz  $Z^2$  scaling [lower dashed line shows  $\lambda = A\alpha^2 Z^2$  Ry with  $A = 0.10$  and  $\alpha$  being the fine structure constant (see text)]. The angular momentum states are color coded, with the  $p$  series in blue,  $d$  in red, and  $f$  in green.

Unlike a similar figure we presented elsewhere [36], Fig. 10 is more complete, in the sense that it includes the SOC of the  $p$  electrons in addition to the  $d$  and the  $f$  electrons. As seen from the figure, phosphorus with  $Z = 15$ , has the SOC strength  $\lambda = 36$  meV [40].

The Rashba effect, for which both SOC and broken inversion symmetry (caused by the applied electric field) is necessary, is described by the Hamiltonian [33,34]

$$H_R = \alpha_R (\vec{\sigma} \times \vec{k}) \cdot \hat{z} = \alpha_R (k_y \sigma_x - k_x \sigma_y) \quad (\text{isotropic case}), \quad (3)$$

where  $\vec{k}$  is the momentum of the electron,  $\vec{\sigma}$  is the Pauli matrix,  $\hat{z}$  is the unit vector along the electric field, and  $\alpha_R$  is the Rashba coefficient. The Hamiltonian Eq. (3) can be readily diagonalized to yield the spin splitting  $\Delta E = 2\alpha_R k$ . Here, the magnitude of the splitting depends on the magnitude of  $\vec{k}$ , but not on the direction (isotropic Rashba splitting), while for the monolayer BP, as we discuss below, the splitting is direction dependent (anisotropic Rashba), and, consequently Eq. (3) will need to be modified.

*Free-electron derivation of the Rashba Hamiltonian (isotropic case).* We outline the naïve derivation of the Rashba Hamiltonian, Eq. (3), for the free electron gas in the presence of an electric field and then extend it to the case where the mass is anisotropic. In many solids, like in BP, the band mass is anisotropic, and the analysis below suggests that in that case, the Rashba splitting should show an anisotropic behavior as well.

The Rashba effect is a relativistic effect, originating from the SOC. In its rest frame, the electron experiences the magnetic field  $\vec{B} = (-\vec{v} \times \vec{E})/c^2$  due to the applied electric field, which then couples to the spin magnetic moment of



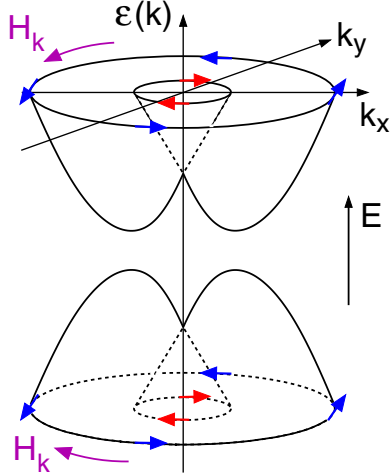


FIG. 11. (Color online) Rashba-split conduction and valence bands (schematic). In the anisotropic mass case, the constant energy contours are ellipses, not circles, and the spins turn along directions tangential to the ellipses. The effective Rashba magnetic fields, Eq. (8), are also indicated.

the electron,  $H_R = -\vec{M} \cdot \vec{B} = -(g\mu_B\vec{\sigma}/2) \cdot (-\vec{v} \times \vec{E}/c^2) = -\vec{H}_k \cdot \vec{\sigma}$ , where

$$\vec{H}_k \equiv -\hbar^2 E |e| (2m^2 c^2)^{-1} (\vec{k} \times \hat{z}). \quad (4)$$

In essence, the applied electric field has been converted into the effective, momentum-dependent magnetic field  $\vec{H}_k$ , which aligns the spins along it and causes the spin eigenstates to turn as indicated in Fig. 11. Rearranging terms, we immediately retrieve the Rashba Hamiltonian  $H_R$  for the isotropic case, Eq. (3), where the Rashba coefficient

$$\alpha_R = \hbar^2 E |e| (2m^2 c^2)^{-1}. \quad (5)$$

We note that while the Rashba splitting has been observed in solids, its magnitude is typically several orders of magnitude higher than predicted from the free-electron result, Eq. (5). This is because in the solid the nuclear fields—which are huge as compared to the applied electric fields in the laboratory or even the fields present near the surfaces of a solid—cause a large enhancement of  $\alpha_R$ . However, an external electric field is still needed to break the inversion symmetry, without which symmetry demands that there would be no spin splitting, viz.,  $\varepsilon_{\vec{k}\sigma} = \varepsilon_{\vec{k}-\sigma}$ , and, consequently, no Rashba effect. Furthermore, while in the naïve derivation outlined above,  $\sigma$  is the real spin of the electron, in the solid due to the spin-orbit coupling,  $\sigma$  in Eq. (3) could represent an entangled spin-orbital state, or a pseudospin, e.g.,  $|\uparrow\rangle \equiv 3^{-1/2} |xy \downarrow - yz \uparrow + ixz \uparrow\rangle$ . These ideas are well known in the literature and developed further in our recent work on the Rashba effect in the  $d$  electron solids [36,41].

**Rashba Hamiltonian (anisotropic case).** Now, consider the case with an anisotropic mass, with the effective mass tensor  $[m^{*-1}(\vec{k})]_{ij} = \hbar^{-2} \partial^2 \varepsilon(\vec{k}) / \partial k_i \partial k_j$  and the velocity  $v_i = \hbar^{-1} \partial \varepsilon(\vec{k}) / \partial k_i = \hbar \sum_j [m^{*-1}]_{ij} k_j$ . A straightforward generalization of the isotropic case yields the desired anisotropic

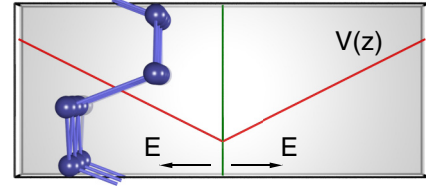


FIG. 12. (Color online) Electric field configuration used in the DFT calculations. Length of the supercell used in the calculation is about twice larger than what is shown here.

### Rashba Hamiltonian

$$H_R = \alpha_R (\vec{\sigma} \times \vec{k}') \cdot \hat{z} = \alpha_R (k'_y \sigma_x - k'_x \sigma_y) \quad (\text{general case}), \quad (6)$$

where  $k'_i = \sum_l (\frac{m}{m^*})_{il} k_l$  and  $m$  is the bare electron mass.

It is easy to show that if the mass tensor can be written as a diagonal matrix with momentum-independent masses, with a principal axis transformation, if needed, so that the constant energy contours are ellipses,  $\hbar^2 k_x^2 / 2m_x + \hbar^2 k_y^2 / 2m_y = \text{const.}$ , then Eq. (6) leads to the spin splitting:

$$\Delta E = 2\alpha_R (m_y^{-2} \sin^2 \theta + m_x^{-2} \cos^2 \theta)^{1/2} k, \quad (7)$$

where the effective masses  $m_x$  and  $m_y$  here are in units of the bare mass  $m$ , and  $\theta = \tan^{-1}(k_y/k_x)$  is the polar angle in the momentum space. Additionally, in this case, the spins point in a direction tangential to the constant-energy ellipses in the momentum space. Analogous to the isotropic case, the Rashba Hamiltonian can be written in the form  $H_R = -\vec{H}_k \cdot \vec{\sigma}$ , with the effective magnetic field

$$\vec{H}_k = -\alpha_R (\vec{k}' \times \hat{z}), \quad (8)$$

which orients the spins along the directions tangential to the constant energy ellipses.

**DFT results for Rashba splitting.** We have computed the electric field effects by applying an electric field normal to the monolayer BP, with the unit cell configuration sketched in Fig. 12, and using the density-functional methods already described.

Figure 13 shows the band structure for the valence top and conduction bottom in the presence of the electric field along specific directions in the BZ, and Fig. 14 shows the Rashba splitting for the conduction band in the  $k_x$ - $k_y$  plane as a contour plot, indicating the anisotropic behavior of the Rashba splitting. Contours for the Rashba splitting of the valence top show similar anisotropic behavior, but are not shown in the figure.

The Rashba splitting shows the anticipated linear- $k$  dependence for both valence and conduction bands as seen from Fig. 15. The slope yields an effective, direction-dependent Rashba coefficient,  $\alpha_R^{\text{eff}} = \alpha_R (m_y^{-2} \sin^2 \theta + m_x^{-2} \cos^2 \theta)^{1/2}$ . The numerical values of  $\alpha_R^{\text{eff}}$  are: (i) valence top,  $\alpha_R^v(x) = 10.9$ ,  $\alpha_R^v(y) = 3.6$ ; and (ii) conduction bottom,  $\alpha_R^c(x) = 14.0$ ,  $\alpha_R^c(y) = 1.7$ , all in units of  $\text{meV} \cdot \text{\AA}$ . These are consistent with the free-electron result that the larger the effective mass, the smaller is the  $\alpha_R^{\text{eff}}$ ; however, the inverse square dependence on the effective mass, which comes from  $\alpha_R$ , is not obeyed. The reason for this is that the simple free-electron model misses

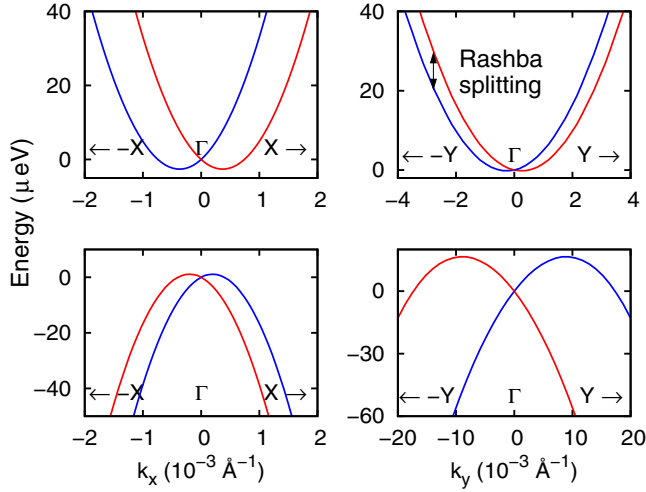


FIG. 13. (Color online) Rashba splitting of the valence top (bottom row) and the conduction bottom (top row) computed from DFT. Left figures show the Rashba splitting along  $k_x$ , while the right figures show the same along  $k_y$ . The electric field used here is  $2.6 \text{ V/Å}$ .

the intricate band structure and the orbital dependent effects in the solid, which are better captured in a tight-binding model [41,42].

As already pointed out,  $\vec{\sigma}$  represents the pseudospin describing the two partner functions in the two Rashba bands, which could be spin-orbital entangled states [41]. In the present case of BP, however, since the SOC is small and the energies of the  $p_x$  and  $p_y$  states that would spin-orbit couple to the  $p_z$  orbitals making up the valence and conduction band extrema are far away in energy, the pseudospins are nearly spin pure states  $|p_z \uparrow\rangle$  and  $|p_z \downarrow\rangle$ .

From the DFT calculations, we have computed the spin wave functions of the Rashba split valence band states in the presence of the electric field and from there, obtained the spin orientation, by simply looking at the wave function at the center of the interplanar P-P bond. The results are shown in Fig. 16. The spin directions are approximately along the anticipated directions, viz., tangential to the ellipses; the small deviation from this is due to the fact that the mass tensor

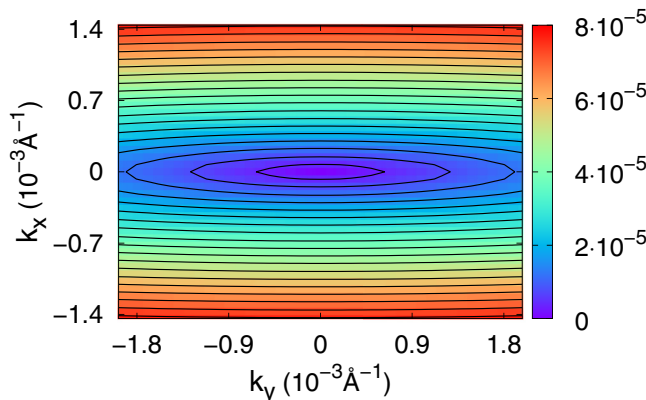


FIG. 14. (Color online) Contour plot of the Rashba splitting for the conduction bottom in the  $k_x$ - $k_y$  plane, indicating anisotropic behavior. Color codes are in eV.

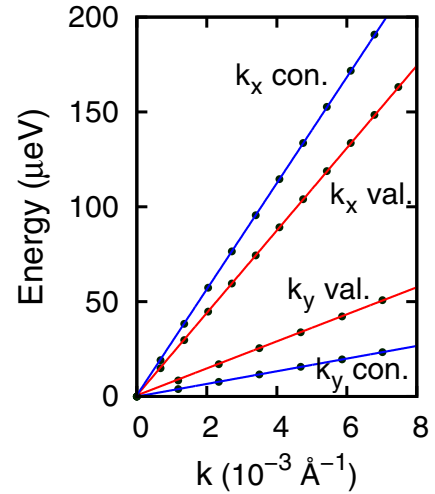


FIG. 15. (Color online) Rashba splitting corresponding to Fig. 13 along  $k_x$  or  $k_y$  directions, showing the linear momentum dependence. Lines are fits to the DFT calculated values, which are shown as points.

is momentum dependent and could have the principal axes oriented in slightly different directions at different  $k$  points, as is evident from Fig. 9, especially as one goes away from the  $\Gamma$  point. Thus, the predictions of the anisotropic Rashba Hamiltonian, Eq. (6), is more or less obeyed by the DFT results for BP.

#### IV. SUMMARY

In summary, we studied the electronic structure of the monolayer BP, both without and with the presence of an applied electric field. Symmetry analysis of the calculated band structure using density-functional methods showed the nature of the chemical bonding to be due to the formation of phosphorus  $p$ - $p$  bonds and provided justification for developing a simple tight-binding model to describe the band structure in terms of just one orbital per atom and using nearest-neighbor

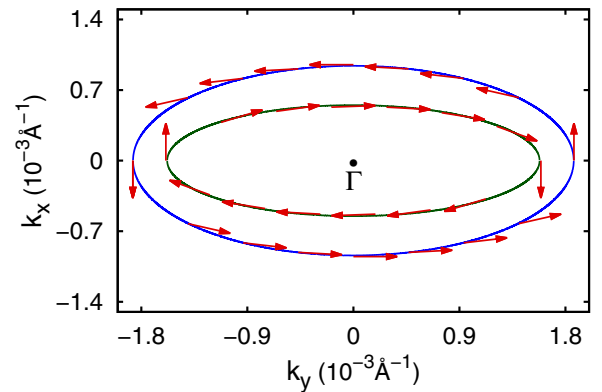


FIG. 16. (Color online) Spin orientations of the Rashba states at the conduction band bottom as computed from the DFT spin wave functions. The spins point along the directions more or less tangential to the ellipses, in agreement with the anisotropic Rashba Hamiltonian Eq. (6). The two ellipses describe the isoenergy surface corresponding to a certain energy, which can be read off using Fig. 13.



interaction only. We then studied the electronic structure in the presence of an applied electric field using density-functional methods, which leads to the Rashba effect. A byproduct of our work was the demonstration that the strength of the spin-orbit coupling in the atoms increases as the square of the atomic number  $Z^2$ , i.e., the Landau-Lifshitz scaling, if we consider the outermost electrons in the atom, which are the relevant valence electrons. In contrast, the hydrogenic  $Z^4$  scaling is obeyed, if we keep the principal and the angular momentum quantum numbers  $n, l$  fixed. In the monolayer BP, both conduction and valence bands show the linear momentum-dependent Rashba splitting. However, the strength of the splitting is anisotropic, depending on the direction of  $\vec{k}$ , and the basic origin of the anisotropy can be explained within the free-electron model, using an anisotropic effective mass. The anisotropic Rashba effect predicted here has never been observed. It would be gratifying to observe the effect from experiments, an effect that could have possible novel uses in spintronics applications.

### ACKNOWLEDGMENTS

This research was supported by the US Department of Energy, Office of Science, under Award No. DE-FG02-00ER45818.

TABLE IV. Character table for the  $D_{2h}$  group, the symmetry group of the Bloch states at the  $\Gamma$  point in the Brillouin zone of BP. The eight symmetry elements of the group are: identity operator  $E$ , space inversion  $I$ , three rotations (proper or improper), viz.,  $\tau C_{2x}, C_{2y}, \tau C_{2z}$ , with the fractional translation  $\tau = (a/2, b/2)$ , and the three reflections (again, proper or improper), viz.,  $\tau R_x, R_y$ , and  $\tau R_z$ . These symmetry elements are best visualized by using Fig. 4.

	$E$	$\tau C_{2x}$	$C_{2y}$	$\tau C_{2z}$	$I$	$\tau R_x$	$R_y$	$\tau R_z$
$\Gamma_1^+$	1	1	1	1	1	1	1	1
$\Gamma_2^+$	1	-1	1	-1	1	-1	1	-1
$\Gamma_3^+$	1	1	-1	-1	1	1	-1	-1
$\Gamma_4^+$	1	-1	-1	1	1	-1	-1	1
$\Gamma_1^-$	1	1	1	1	-1	-1	-1	-1
$\Gamma_2^-$	1	-1	1	-1	-1	1	-1	1
$\Gamma_3^-$	1	1	-1	-1	-1	-1	1	1
$\Gamma_4^-$	1	-1	-1	1	-1	1	1	-1

### APPENDIX: CHARACTER TABLE FOR $D_{2h}$

We have used the same symmetry notations as earlier authors [23,24], which are given here in Table IV to make the discussions self-contained.

- [1] A. K. Geim, *Science* **324**, 1530 (2009).
- [2] A. H. Castro Neto and K. Novoselov, *Rep. Prog. Phys.* **74**, 082501 (2011).
- [3] K. S. Novoselov, A. K. Geim, S. V. Morozov, D. Jiang, Y. Zhang, S. V. Dubonos, I. V. Grigorieva, and A. A. Firsov, *Science* **306**, 666 (2004).
- [4] B. Aufray, A. Kara, S. Vizzini, H. Oughaddou, C. Landri, B. Ealet, and G. Le Lay, *Appl. Phys. Lett.* **96**, 183102 (2010).
- [5] B. Lalami, H. Oughaddou, H. Enriquez, A. Kara, S. Vizzini, B. Ealet, and B. Aufray, *Appl. Phys. Lett.* **97**, 223109 (2010).
- [6] M. E. Dvila, L. Xian, S. Cahangirov, A. Rubio, and G. L. Lay, *New J. Phys.* **16**, 095002 (2014).
- [7] A. Morita, *Appl. Phys. A* **39**, 227 (1986).
- [8] H. Liu, Y. Du, Y. Deng, and P. D. Ye, *Chem. Soc. Rev.* **44**, 2732 (2015).
- [9] F. Xia, H. Wang, and Y. Jia, *Nature Commun.* **5**, 4458 (2014).
- [10] R. W. Keyes, *Phys. Rev.* **92**, 580 (1953).
- [11] D. Warschauer, *J. Appl. Phys.* **34**, 1853 (1963).
- [12] Y. Akahama, S. Endo, and S. Narita, *Physica B+C* **139-140**, 397 (1986).
- [13] T. Kikegawa and H. Iwasaki, *Acta Crystallogr., Sec. B: Struct. Sci.* **39**, 158 (1983).
- [14] J. C. Jamieson, *Science* **139**, 1291 (1963).
- [15] L. Cartz, S. R. Srinivasa, R. J. Riedner, J. D. Jorgensen, and T. G. Worlton, *J. Chem. Phys.* **71**, 1718 (1979).
- [16] H. Liu, A. T. Neal, Z. Zhu, Z. Luo, X. Xu, D. Tomnek, and P. D. Ye, *ACS Nano* **8**, 4033 (2014).
- [17] W. Lu, H. Nan, J. Hong, Y. Chen, C. Zhu, Z. Liang, X. Ma, Z. Ni, C. Jin, and Z. Zhang, *Nano Research* **7**, 853 (2014).
- [18] A. N. Rudenko and M. I. Katsnelson, *Phys. Rev. B* **89**, 201408 (2014).
- [19] R. Wyckoff, *Crystal Structures*, Vol. 1 (Wiley, New York, 1963).
- [20] P. Blaha, K. Schwarz, G. Madsen, D. Kvasnicka, and J. Luitz, *WIEN2k: An Augmented Plane Wave plus Local Orbitals Program for Calculating Crystal Properties* (Institute of Physical and Theoretical Chemistry, Vienna, 2001).
- [21] J. P. Perdew, K. Burke, and M. Ernzerhof, *Phys. Rev. Lett.* **77**, 3865 (1996).
- [22] J. Qiao, X. Kong, Z.-X. Hu, F. Yang, and W. Ji, *Nature Commun.* **5**, 4475 (2014).
- [23] P. Li and I. Appelbaum, *Phys. Rev. B* **90**, 115439 (2014).
- [24] Y. Takao, H. Asahina, and A. Morita, *J. Phys. Soc. Jpn.* **50**, 3362 (1981).
- [25] A. S. Rodin, A. Carvalho, and A. H. Castro Neto, *Phys. Rev. Lett.* **112**, 176801 (2014).
- [26] I. Shirovani, *Mol. Crystals Liq. Crystals* **86**, 203 (1982).
- [27] S. Narita, Y. Akahama, Y. Tsukiyama, K. Muro, S. Mori, S. Endo, M. Taniguchi, M. Seki, S. Suga, A. Mikuni *et al.*, *Physica B+C* **117-118**, 422 (1983).
- [28] Y. Akahama, S. Endo, and S. Narita, *J. Phys. Soc. Jpn.* **52**, 2148 (1983).
- [29] H. Y. Lv, W. J. Lu, D. F. Shao, and Y. P. Sun, *arXiv:1404.5171v1*.
- [30] M. Gmitra, S. Konschuh, C. Ertler, C. Ambrosch-Draxl, and J. Fabian, *Phys. Rev. B* **80**, 235431 (2009).
- [31] J. Balakrishnan, G. Kok Wai Koon, M. Jaiswal, A. H. Castro Neto, and B. Ozyilmaz, *Nature Phys.* **9**, 284 (2013).
- [32] S. V. Eremin, I. A. Nechaev, P. M. Echenique, and E. V. Chulkov, *Sci. Rep.* **4**, 6900 (2014).

- [33] E. I. Rashba, *Sov. Phys. Solid. State* **2**, 1109 (1960).
- [34] Y. A. Bychkov and E. I. Rashba, *J. Phys. C: Solid State Phys.* **17**, 6039 (1984).
- [35] L. Landau and E. Lifshitz, *Quantum Mechanics: Non-Relativistic Theory*, Course of Theoretical Physics (Elsevier Science, Amsterdam, 1981).
- [36] K. V. Shanavas, Z. S. Popović, and S. Satpathy, *Phys. Rev. B* **90**, 165108 (2014).
- [37] F. Herman and S. Skillman, *Atomic Structure Calculations* (Prentice-Hall, New Jersey, 1963).
- [38] O. K. Andersen, O. Jepsen, and D. Glötzel, *Highlights of Condensed Matter Theory*, Proceedings of The International School of Physics Enrico Fermi, edited by F. Bassani, F. Fumi, and M. P. Tosi, Vol. 190 (North Holland, New York, 1985).
- [39] G. Shortley and E. Condon, *The Theory of Atomic Spectra* (Cambridge University Press, Cambridge, 1951).
- [40] J. Desclaux, *At. Data Nucl. Data Tables* **12**, 311 (1973).
- [41] K. V. Shanavas and S. Satpathy, *Phys. Rev. Lett.* **112**, 086802 (2014).
- [42] L. Petersen and P. Hedegrd, *Surf. Sci.* **459**, 49 (2000).